Science
AAAS

**Epitaxial BiFeO3 Multiferroic Thin Film Heterostructures**
J. Wang, *et al.*
*Science* **299**, 1719 (2003);
DOI: 10.1126/science.1080615



*Science* (print ISSN 0036-8075; online ISSN 1095-9203) is published weekly, except the last week in December, by the American Association for the Advancement of Science, 1200 New York Avenue NW, Washington, DC 20005. 

# Epitaxial $BiFeO_3$ Multiferroic Thin Film Heterostructures

J. Wang,[1] J. B. Neaton,[2]† H. Zheng,[1]† V. Nagarajan,[1] S. B. Ogale,[3] B. Liu,[1] D. Viehland,[4] V. Vaithyanathan, [5] D. G. Schlom,[5] U. V. Waghmare,[6] N. A. Spaldin,[7] K. M. Rabe,[2] M. Wuttig,[1] R. Ramesh[3]*

**Enhancement of polarization and related properties in heteroepitaxially constrained thin films of the ferroelectromagnet, $BiFeO_3$, is reported. Structure analysis indicates that the crystal structure of film is monoclinic in contrast to bulk, which is rhombohedral. The films display a room-temperature spontaneous polarization (50 to 60 microcoulombs per square centimeter) almost an order of magnitude higher than that of the bulk (6.1 microcoulombs per square centimeter). The observed enhancement is corroborated by first-principles calculations and found to originate from a high sensitivity of the polarization to small changes in lattice parameters. The films also exhibit enhanced thickness-dependent magnetism compared with the bulk. These enhanced and combined functional responses in thin film form present an opportunity to create and implement thin film devices that actively couple the magnetic and ferroelectric order parameters.**

Materials that have coupled electric, magnetic, and structural order parameters that result in simultaneous ferroelectricity, ferromagnetism, and ferroelasticity are known as multiferroics (*1*, *2*). These compounds present opportunities for potential applications in information storage, the emerging field of spintronics, and sensors. There has been recent research interest in a number of prototypical magnetic ferroelectrics, including $YMnO_3$, a hexagonal perovskite that is antiferromagnetic [Neél temperature ($T_N$) between 70 and 130 K] and ferroelectric [Curie temperature ($T_C$) between 570 and 990 K] in the ground state (*3*, *4*), and $BiMnO_3$, a monoclinic perovskite that is both ferromagnetic ($T_N \sim 100$ K) and ferroelectric ($T_C \sim 450$ K) (*5*– *7*). The perovskite $BiFeO_3$ is ferroelectric ($T_C \sim 1103$ K) and antiferromagnetic ($T_N \sim 643$ K), exhibiting weak magnetism at room temperature due to a residual moment from a canted spin structure (*2*). The structure and properties of the bulk single crystal form have been extensively studied (*8*–*13*), and it has been shown to possess a rhombohedrally distorted perovskite structure ($a = b = c = 5.63$ Å, $\alpha = \beta = \gamma = 59.4°$) at room temperature. In single crystals, the spontaneous polarization ($P_s$) is 3.5 microcoulombs per square centimeter ($\mu C/cm^2$) along the (001) direction, indicating a value of 6.1 $\mu C/cm^2$ along the (111) direction at 77 K (*10*). Transport measurements in the bulk have been hampered by leakage problems, likely a result of defects and nonstoichiometry, which have limited the applications of this material. To overcome this obstacle, recent work has focused on solid solutions of $BiFeO_3$ with other $ABO_3$ (where A is the cation at the vertices of the cube and B is the cation at the body center) materials, such as $BaTiO_3$, which can prevent second-phase formation and increase sample resistivity. For example, Ueda *et al*. reported a remanent polarization of 2.5 $\mu C/cm^2$ in a $(Bi_{0.7}Ba_{0.3})(Fe_{0.7}Ti_{0.3})O_3$ film (*14*).

An important aspect that emerges upon examination of the properties of bulk $BiFeO_3$ (single crystal or ceramic) is that the parent compound has a spontaneous polarization value that is significantly smaller than the expected value for a ferroelectric with such a high $T_C$ (for example, lead titanate, with a $T_C$ of ~763 K, has a spontaneous polarization of 80 to 100 $\mu C/cm^2$.) Indeed, this anomaly has been noted in an earlier report (*10*). It is not clear whether this is a result of intrinsic material properties or of limitations imposed by leakage and imperfect material quality in bulk. The resolution of this issue was the initial motivation of this study, which focuses on creating a model thin-film $BiFeO_3$ system by using oxide heteroepitaxy.

In our experiments, we grew phase-pure $BiFeO_3$ (BFO) thin films in the thickness range of 50 to 500 nm by pulsed laser deposition (PLD) onto single crystal $SrTiO_3$(100) (STO) substrates. To ensure heteroepitaxial growth, we chose the conducting perovskite oxide electrode, $SrRuO_3$ (SRO) (*15*) [see supporting online material (SOM) text for growth and characterization details].

Large angle x-ray scans (20° to 80°) showed only diffraction peaks from the substrate and (00l) pseudocubic reflections from the heterostructure. We did not observe any reflections that would be indicative of second phases. A small section of the x-ray diffraction spectra from films of varying thickness (Fig. 1A) demonstrates the dependence of the BFO out-of-plane lattice parameter on film thickness (Fig. 2D). Selected area electron diffraction (SAED) patterns (Fig. 1B), as well as low-magnification bright field images, obtained from a (100) cross section confirm the single crystalline quality of the BFO layer. Analysis of the SAED pattern from a 200-nm sample reveals that the (010) and (001) reflections have different spacings, yielding a ratio of 1.016. Indexing of this SAED pattern with pseudocubic indices yields an in-plane

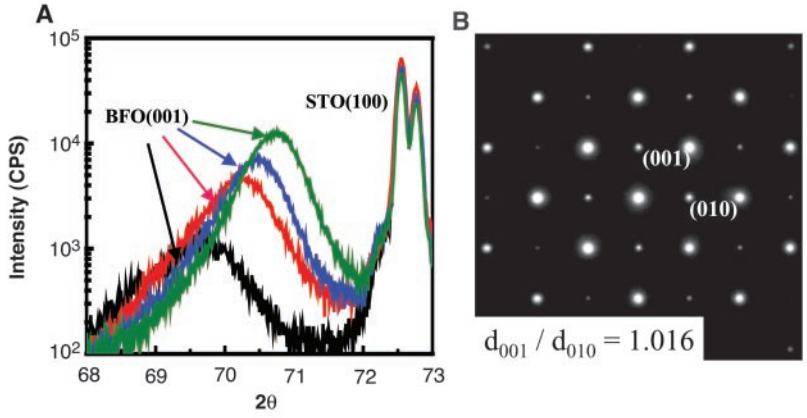


**Fig. 1.** (**A**) (003) peaks from x-ray θ-2θ scans showing the effect of film thickness on heteroepitaxial strain. As the film thickness is increased from 70 to 400 nm, the peak position progressively increases (black line, 70 nm; red line, 100 nm; blue line, 200 nm; and green line, 400 nm), indicating a decrease of the out-of-plane lattice parameter. (**B**) The SAED pattern confirms the structure distortion.

[1]Department of Materials Science and Engineering, University of Maryland, College Park, MD 20742, USA. [2]Department of Physics and Astronomy, Rutgers University, Piscataway, NJ 08854, USA. [3]Department of Physics, University of Maryland, College Park, MD 20742, USA. [4]Department of Materials Science and Engineering, Virginia Polytechnic Institute, Blacksburg, VA 24061, USA. [5]Department of Materials Science and Engineering, Pennsylvania State University, University Park, PA 16802–5055, USA. [6]J. Nehru Centre for Advanced Scientific Research, Jakkur, Bangalore 560 064, India. [7]Materials Department, University of California, Santa Barbara, CA 94805, USA.

*To whom correspondence should be addressed. E-mail: rr136@umail.umd.edu

†These authors contributed equally to this work.

parameter of 3.935 Å and an out-of-plane parameter of 4.0 Å. Careful analysis of the crystal structure using four-circle x-ray diffraction suggests a tetragonal-like crystal structure with the c axis normal to the substrate surface, with a small monoclinic distortion of about 0.5°. These experimental observations can be interpreted as a consequence of a compressive stress imposed by the SRO electrode, which has an in-plane lattice parameter smaller than that of BFO. These results lead to two key observations: (i) heteroepitaxial, in-plane compressive stress imposed by the epitaxial bottom electrode allows growth of a monoclinic crystal structure in BFO, and (ii) the degree of compressive stress progressively decreases with increasing BFO thickness (as expected).

We investigated the effect of this constrained crystallographic state in the BFO layer on its physical properties. Ferroelectric properties were characterized using polarization hysteresis and pulsed polarization measurements. In the hysteresis loop that we measured at a frequency of 15 kHz for the 200-nm-thick film (Fig. 2A), the observed remanent polarization ($P_r$, 50 to 60 μC/cm$^2$) is an order of magnitude higher than the highest reported value of 6.1 μC/cm$^2$ from bulk BFO. To confirm this result, we measured the polarization characteristics under a pulsed probe condition, which is less likely to be convoluted by leakage and nonlinear dielectric effects. The pulsed remanent polarization (defined as $\Delta P = P^* - P^\wedge \approx 2P_r$, where $P^*$ is the switched polarization and $P^\wedge$ is the nonswitched polarization) [measured using 10-μs wide pulses (Fig. 2B)] shows a sharp increase of $\Delta P$ about 15 megavolts (MV) per meter, reaching a value of about 100 μC/cm$^2$ at 55 MV/m. The films display resistivity values of ~$10^9$ ohm·cm, which is comparable to values obtained for epitaxial Ti-rich lead zirconate titanate (PZT) films**.** This polar state was found to be stable, as evidenced by polarization retention experiments conducted over several days. Additional support for the spontaneous polar state comes from piezoelectric measurements. The piezoelectric hysteresis loop (Fig. 2C), measured using a scanning force microscope (see SOM text for technique details), shows a remanent out-of-plane piezoelectric coefficient ($d_{33}$) value of 70 pm/V, representing the piezoresponse of the film in the fully clamped state, which is comparable to the value obtained from Ti-rich PZT films (Zr/Ti ratio of 20/80) (*16*). Figure 2D summarizes the thickness dependence of the polarization and piezoelectric coefficient. The polarization increases and the $d_{33}$ value decreases as the film thickness is decreased. The small signal out-of-plane dielectric constant ($\varepsilon_{33}$) follows the same trend as the $d_{33}$ measurements. In the case of epitaxial $PbTiO_3$ and $BaTiO_3$ films, in-plane compressive stresses lead to a decrease of $\varepsilon_{33}$, along with an enhancement of the spontaneous polarization (*17*). The thickness dependence observed (Fig. 2D) can be similarly understood as a direct consequence of the induced compressive stress imposed by heteroepitaxy.

To understand the experimental data at the atomic level, we turned to first-principles calculations of total energy and polarization. These calculations were carried out within a local spin-density approximation (LSDA) with a plane wave basis set and projector-augmented wave pseudopotentials using the Vienna Ab-initio Simulation Package (VASP) (*18*–*20*). [All calculations have been verified with another plane wave-pseudopotential package, ABINIT (*21*).] For a number of ferroelectric oxides, the spontaneous polarization has been accurately computed from first principles (*22*) using the Berry-phase formalism (*23*, *24*). For a given structure, this determines a discrete set of allowed values for the electronic contribution to the polarization $\mathbf{P}_{el} + 2e\mathbf{R}/\Omega$, where $\mathbf{R}$ is a lattice vector, $\Omega$ is the unit cell volume, and $e$ is the charge of the electron. The possible values for the change in total polarization with switching (equal to twice the spontaneous polarization) $P_S$ are therefore $2\mathbf{P}_0 + 2e\mathbf{R}/\Omega$. Here, we report a single value for spontaneous polarization, $P_S$, parallel to a given direction.

We first investigated the bulk rhombohedral phase by optimizing the structural parameters of $BiFeO_3$ in a 10-atom unit cell with space group R3c (Fig. 3A). The structure can be described as a distorted perovskite. The ground state was found to be an antiferromagnetic insulator with a lattice constant of 5.459 Å and a rhombohedral angle of 60.36°, as compared with the experimental values 5.6343 Å and 59.348° (*13*), which are within the deviations typical of the LSDA. The absence of centrosymmetry in R3c permits the relative displacements of the atomic sublattices along (111), most notably those of Bi with respect to the distorted $FeO_6$ cages. The minimum energy structure has values of these displacements in excellent agreement with the experimental structural determinations. The Berry-phase calculation yields a spontaneous polarization of +6.61 μC/cm$^2$ along (111), in excellent agreement with the reported bulk value of 6.1 μC/cm$^2$.

For the thin-film phase, we considered a tetragonal structure based on the cubic perovskite structure with symmetry lowered to *P*4*mm* (i.e., we neglected the small monoclinic distortion). The lattice parameters were fixed to the pseudotetragonal parameters measured for the 200-nm film ($a$ = 3.935Å and $c/a$ = 1.016). Computations were performed with a body-centered tetragonal unit cell, which was necessary to accommodate the G-type antiferromagnetic ordering. The key results of our calculations for the thin film are shown in Fig. 3, C and D. The magnitudes of the ionic displacements relative to the centrosymmetric strained perovskite structure were found to be extremely large: relative to the Bi ion, the Fe (Wyckoff position 4b) and apical O (4b) are displaced

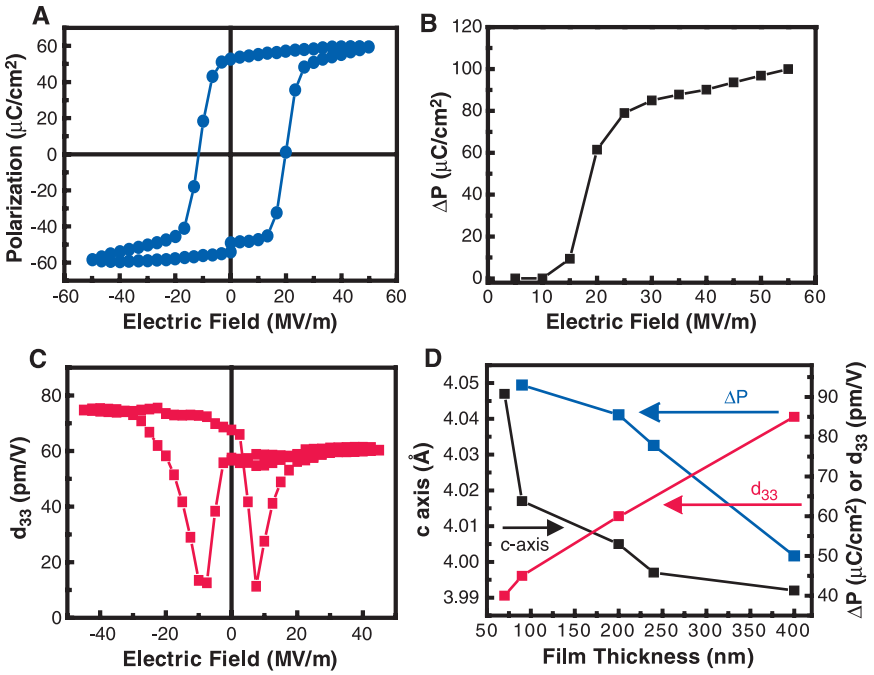


**Fig. 2.** (**A**) A ferroelectric hysteresis loop measured at a frequency of 15 kHz, which shows that the film is ferroelectric with $P_r \sim 55$ μC/cm$^2$. (**B**) Pulsed polarization $\Delta P$ versus electric field measured with electrical pulses of 10-μs width. (**C**) A small signal $d_{33}$ for a 50-μm capacitor. (**D**) A summary of the thickness dependence of out-of-plane lattice parameter, polarization, and $d_{33}$. The small signal dielectric constant (*27*) follows the same trend as the $d_{33}$.

by about 9% (of the *c* axis parameter) and 13%, respectively, and the equatorial O atoms (8c) by nearly 18%. (Figure 3B is a schematic tetragonal $BiFeO_3$ unit cell.) The Fe displacement along the Fe-O(4b) chain is negligible, whereas the oxygen octahedron is distorted by relative displacement of the equatorial and apical oxygens. The Berry-phase calculation yields a spontaneous polarization of $+63.2\ \mu C/cm^2$ along (001), which is consistent with the experimentally observed large values of polarization of our (001)-oriented films. Although there may be other tetragonal structures that are lower in energy (the energy per unit cell is about 0.4 eV per formula unit greater than the optimized rhombohedral structure), this result shows that a dramatically different polarization can be obtained with a relatively small change in the lattice parameters.

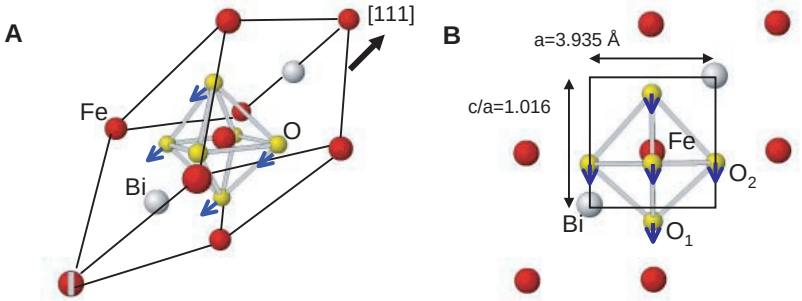


C

Rhombohedral R3c ($P_s$ || [111])

| | LSDA | Expt |
|---|---|---|
| Bi (2a) *x* | 0 | 0 |
| Fe (2a) *x* | 0.2308 | 0.22077 |
| O (6b) *x* | 0.5423 | 0.5279 |
| *y* | 0.9428 | 0.9333 |
| *z* | 0.3980 | 0.3948 |
| a (Å) | 5.4590 | 5.6343 |
| α (°) | 60.36 | 59.348 |
| V (Å$^3$) | 115.98 | 124.601 |
| **$P_s$(μC/cm$^2$)** | **6.61** | **6.1** |

D

Tetragonal P4mm ($P_s$ || [001])

| | LSDA | Expt |
|---|---|---|
| Bi (1a) *z* | 0 | |
| Fe (1b) *z* | 0.41 | |
| $O_1$ (1b) *z* | -0.101 | |
| $O_2$ (2c) *z* | 0.367 | |
| a (Å) | 3.935* | 3.935 |
| c/a | 1.016* | 1.016 |
| V (Å$^3$) | 61.91* | 61.91 |
| **$P_s$(μC/cm$^2$)** | **63.2** | **50-60** |

**Fig. 3.** Schematic of the prototypical rhombohedral (**A**) and tetragonal (**B**) $BiFeO_3$ unit cells. (Note that computations were performed with a 10-atom body-centered tetragonal unit cell, which was doubled to accommodate the G-type antiferromagnetic ordering.) The corresponding atomic positions and spontaneous polarizations from first-principles calculations are shown in (**C**) and (**D**), respectively. Structural parameters for the rhombohedral R3c phases were taken from (*13*). The asterisks in (D) indicate that lattice parameters were fixed to the experimental values of the 200-nm film.

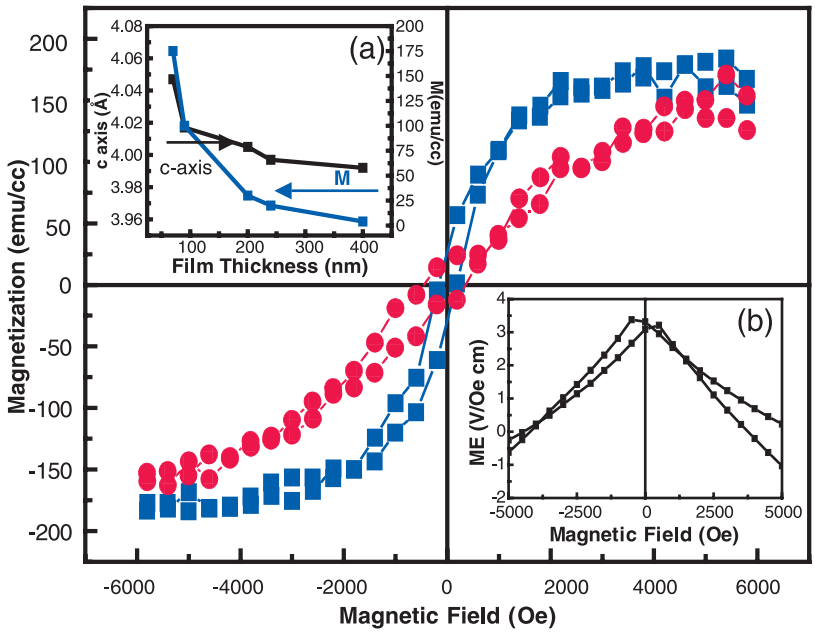


**Fig. 4.** Magnetic hysteresis loops measured by vibrating sample magnetometry for a 70-nm-thick BFO film, showing an appreciable saturation magnetization of ~150 emu/cm$^3$ and a coercive field of ~200 Oe. The in-plane loop is shown in blue, and the out-of-plane loop is in red. Inset (a) shows the thickness dependence of saturation magnetization, illustrating the effect of heteroepitaxial constraint. Inset (b) is a preliminary ME measurement result showing a maximum value of ~3 V/cm·Oe and hysteresis about 200 Oe.

The results demonstrate the influence of heteroepitaxial constraint on the crystal structure and ferroelectric responses in the BFO thin film. We now turn our attention to the magnetic response. The field-dependent magnetization is shown for a 70-nm-thick film (Fig. 4). The Fig. 4 inset (a) shows the thickness dependence of the magnetization. For the thinnest film that we measured (70 nm), the saturation magnetization was ~150 electromagnetic unit (emu)/cm$^3$ (corresponding to ~1 $\mu_B$ per unit cell); as film thickness increases to 400 nm, magnetization decreases to ~5 emu/cm$^3$. The films exhibit enhanced magnetization values as compared to the bulk ceramic (*25*), although the lack of any published data on single crystals precludes any detailed comparative evaluation. The observation of a thickness dependence of the magnetization points to the effect of the mismatch strain on the magnetic response. The coupling of electric and magnetic orders in BFO gives rise to a magnetoelectric (ME) effect. A quasistatic setup (*26*) was used to determine the ME *dE*/*dH* coefficient (where *E* is the electric field and *H* is the magnetic field) of the epitaxial films. The preliminary result, shown in the Fig. 4 inset (b), indicates a *dE*/*dH* coefficient as high as 3 V/cm·Oe at zero field.

Our work presents direct experimental evidence for the heteroepitaxial stabilization of a monoclinic phase with large spontaneous polarization in the ferroelectromagnet system, $BiFeO_3$. These films also show a significant enhancement of magnetization compared with the bulk. A strong piezoelectric response of ~70 pm/V provides the basis for creating lead-free piezoelectrics for sensors and actuators.

### References and Notes


1. E. K. H. Salje, *Phase Transitions in Ferroelastic and Co-elastic Crystals* (Cambridge Univ. Press, Cambridge, 1990).
2. G. A. Smolenskii, I. Chupis, *Sov. Phys. Usp.* **25**, 475 (1982).
3. A. Filippetti, N. A. Hill, *J. Magn. Magn. Mater.* **236**, 176 (2001).
4. M. Fiebig, Th. Lottermoser, D. Frohlich, A. V. Goltsev, R. V. Pisarev, *Nature* **419**, 818 (2002).
5. N. A. Hill, K. M. Rabe, *Phys. Rev. B* **59**, 8759 (1999).
6. R. Seshadri, N. A. Hill, *Chem. Mater.* **13**, 2892 (2001).
7. A. M. dos Santos *et al.*, *Sol. Stat. Comm.* **122**, 49 (2002).
8. C. Michel, J.-M. Moreau, G. D. Achenbach, R. Gerson, W. J. James, *Solid State Commun.* **7**, 701 (1969).
9. J. D. Bucci, B. K. Robertson, W. J. James, *J. Appl. Cryst.* **5**, 187 (1972).

10. J. R. Teague, R. Gerson, W. J. James, *Solid State Commun.* **8**, 1073 (1970).
11. Yu. E. Roginskaya, Yu. Ya. Tomashpol'skii, Yu. N. Venevtsev, V. M. Petrov, G. S. Zhdanov, *Sov. Phys. JETP* **23**, 47 (1966).
12. S. V. Kiselev, R. P. Ozerov, G. S. Zhdanov, *Sov. Phys. Dokl.* **7**, 742 (1963).
13. F. Kubel, H. Schmid, *Acta Crystallogr. B* **46**, 698 (1990).
14. K. Ueda, H. Tabata, T. Kawai, *App. Phys. Lett.* **75**, 555 (1999).
15. C. B. Eom, R. J. Cava, R. M. Fleming, J. M. Phillips, *Science* **258**, 1766 (1992).
16. M. J. Haun, E. Furman, S. J. Jang, L. E. Cross, *Ferroelectrics* **99**, 63 (1989).
17. N. A. Pertsev, A. G. Zembilgotov, A. K. Tagantsev, *Phys. Rev. Lett.* **80**, 1988 (1998).
18. G. Kresse, J. Hafner, *Phys. Rev. B* **47**, 558 (1993).
19. _____, *Phys. Rev. B* **54**, 11169 (1996).
20. G. Kresse, J. Joubert, *Phys. Rev. B* **59**, 1758 (1999).
21. The ABINIT code is a common project of the Université Catholique de Louvain, Corning Incorporated, and other contributors (www.abinit.org). See X. Gonze *et al.*, *Comput. Mater. Sci.* **25**, 478 (2002).
22. W. Zhong, R. D. King-Smith, D. Vanderbilt, *Phys. Rev. Lett.* **72**, 3618 (1994).
23. R. D. King-Smith, D. Vanderbilt, *Phys. Rev. B* **47**, 1651 (1993).
24. D. Vanderbilt, R. D. King-Smith, *Phys. Rev. B* **48**, 4442 (1993).
25. M. Mahesh Kumar, S. Srinath, G. S. Kumar, S. B. Suryanarayana, *J. Magn. Magn. Mater.* **188**, 203 (1998).
26. H. G. Rajaram, thesis, Pennsylvania State University (1991).
27. J. Wang *et al.*, data not shown.

28. We thank L. V. Saraf and V. Kulkarni for help with x-ray diffraction and Rutherford Backscattering measurements. J.B.N. and K.M.R. thank D. Vanderbilt for useful discussions. Supported by the Office of Naval Research (grant MURI N000140110761) and the NSF (grant MRSEC DMR-00-80008. It also benefits from the support of the NSF grant DMR0095166.

**Supporting Online Material**
www.sciencemag.org/cgi/content/full/299/5613/1719/DC1
SOM Text
Figs. S1 and S2
References and Notes

19 November 2002; accepted 3 February 2003

# Taming Winfree Turbulence of Scroll Waves in Excitable Media

**Sergio Alonso,[1] Francesc Sagués,[1] Alexander S. Mikhailov[2]***

**Winfree turbulence of scroll waves is a special kind of spatiotemporal chaos that exists exclusively in three-dimensional excitable media and is currently considered one of the principal mechanisms of cardiac fibrillation. A chaotic wave pattern develops through the negative-tension instability of vortex filaments, which tend to spontaneously stretch, bend, loop, and produce an expanding tangle that fills up the volume. We demonstrate that such turbulence can readily be controlled by weak nonresonant modulation of the medium excitability. Depending on the forcing frequency, either suppression or induction of turbulence can be achieved.**

About 10 years ago, Winfree suggested that three-dimensional (3D) excitable media may possess a special mechanism of wave turbulence, different in principle from the breakup of spiral waves in two dimensions. Spatiotemporal chaos emerges via the disorderly dynamics shown by the vortex filaments of scroll waves, which "snake about, fragment, and close in rings" (*1*). In his view, this process could provide an explanation for the development of fibrillation and the occurrence of sudden cardiac death in healthy people. In subsequent discussion, his analysis of cardiological data was criticized (*2*) and it was also pointed out that sometimes breakup of waves occurs more easily in large volumes than in thin slabs (*3*). Nonetheless, the turbulence described by Winfree has indeed been found in general models of excitable media. Its origin lies in the effect of negative tension of vortex filaments (*4–7*). Such filaments, which represent the cores of rotating scroll waves, tend to stretch themselves and to form loops and complex tangles. This behavior is characteristic for media with relatively low excitability, where the rotation period of spiral waves is large and the medium completely recovers after each propagating wave. In recent realistic simulations of cardiac arrhythmias, this form of fibrillation has been seen under ischemic conditions, in cardiac tissue deprived of oxygen (*8*). Scroll waves are also possible in other excitable media, such as the chemical Belousov-Zhabotinsky reaction (*9*) or the slime mold *Dictyostelium discoideum* (*10*). Experiments on taming excitation waves (*11–13*), oscillatory patterns (*14–15*), and chemical turbulence (*16*) in thin aqueous layers and surface chemical reactions have recently attracted much attention. In excitable 3D media, only the effects of spatial gradients (*17–18*), resonant periodic forcing (*19*), and noise (*20*) on scroll waves have previously been discussed. Here, we show that the Winfree turbulence of scroll waves is amenable to control by uniform periodic forcing. Both suppression and induction of such turbulence, depending on the forcing period, are demonstrated.

In its transverse cross section, a scroll wave looks like a spiral. Such spirals are stacked one upon another to form a scroll-shaped pattern. The scroll rotates around a central filament characterized by zero excitation amplitude. This filament can be straight or curved; it may also form loops and close into contracting or expanding rings. Our analysis is based on the general Barkley model (*21*), whose parameter space is shown in Fig. 1. Inside a broad region, characterized by decreased excitability, expanding scroll rings that give rise to Winfree turbulence were observed. An example of turbulence development is presented in Fig. 2, A to E, where thick yellow lines show the filaments around which scroll waves are rotating. The inhibitor

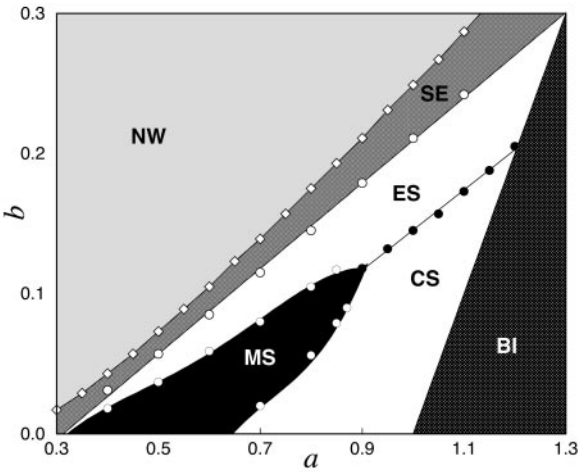


**Fig. 1.** Parameter space of the Barkley model. Evolution of the activator $u$ and inhibitor $v$ variables is governed in this model by two equations: $\partial u/\partial t = \varepsilon^{-1}u(1-u)[u-(v+b)/a)] + \nabla^2 u$ and $\partial v/\partial t = u - v$, where $\varepsilon$ is the ratio of the characteristic activator and inhibitor time scales, $\varepsilon$ is fixed at 0.02 here and $a$ and $b$ are parameters of the model, $b$ determining the excitation threshold. Stable 2D spiral waves are found in numerical simulations inside the entire white region, and meandering of spiral waves takes place in region MS. The 2D medium does not support excitation waves in region NW, is subexcitable (wave fragments shrink) in region SE, and is bistable in region BI. A line divides the white region into the domains where collapsing (CS) and expanding (ES) scroll rings are observed. This boundary was determined by numerical 3D simulations that assume axial symmetry of the rings. The symbols (open and solid dots and squares) indicate the points at which numerical simulations were performed. NW, no waves; SE, subexcitable; MS, meandering spirals; BI, bistable.

[1]Departament de Química Física, Universitat de Barcelona, Avenida Diagonal 647, 08028 Barcelona, Spain. [2]Abteilung Physikalische Chemie, Fritz-Haber-Institut der Max-Planck-Gesellschaft, Faradayweg 4-6, 14195 Berlin, Germany.

*To whom correspondence should be addressed. E-mail: mikhailov@fhi-berlin.mpg.de